Influence of spanwise no-slip boundary conditions on the flow around a cylinder

Håkon Strandenes[1], Bjørnar Pettersen[1], Helge I. Andersson[2], and Michael Manhart[3]

[1] *Department of Marine Technology, Norwegian University of Science and Technology, Otto Nielsens veg 10, 7052 Trondheim, Norway*

[2] *Department of Energy and Process Engineering, Norwegian University of Science and Technology, Kolbjørn Hejes vei 1B, 7034 Trondheim, Norway*

[3] *Professorship of Hydromechanics, Technical University of Munich, Arcisstr. 21, 80333 Munich, Germany*

Corresponding author e-mail: hakon.strandenes@ntnu.no

28th April 2017

Abstract

First we present high resolution large eddy simulations (LES) for the flow past a circular cylinder at Reynolds number 3900 to prove the quality of the simulations. A thorough grid convergence study is presented, and the agreement in the mean flow statistics between our simulations and the references is excellent. Then we apply a no-slip boundary condition at the spanwise boundaries of the cylinder, with aspect ratios of 6, 12 and 24. This results in large changes in the shear layers and wake topology, even for an aspect ratio of 24. Even though the boundary layers along the side walls are only about 0.4 diameters thick, they nevertheless manage to stabilize the shear layers all the way through the channel, thus effectively delaying the roll-up and transition to a turbulent wake.

Keywords: cylinder; LES; no-slip; spanwise boundary; shear layer stability

NOMENCLATURE

C_D	Drag coefficient	Q	Second invariant of ∇u
C_L	Lift coefficient	Re	Reynolds number $Re = DU_\infty/\nu$
C_{pb}	Base pressure coefficient	St	Strouhal number $St = f_v D/U_\infty$
D	Cylinder diameter	u, v, w	Instantaneous fluid velocity
f_v	Vortex shedding frequency	$\overline{U}, \overline{V}, \overline{W}$	Time-averaged fluid velocity
L	Cylinder length	u', v', w'	$u' = u - \overline{U}$ etc.
L_r	Recirculation length	U_∞	Inlet (freestream) velocity
L_v	Vortex formation length	ν	Kinematic viscosity of fluid
ω_z	Vorticity $\omega_z = \partial v/\partial x - \partial u/\partial y$	x, y, z	Cartesian coordinates
p	Pressure	$\overline{\square}$	Time-averaged
P_{uu}	Power spectral density of u-velocity	$\square^{\text{rms}}$	Root-mean-square $= \sqrt{\overline{(\square - \overline{\square})^2}}$

1 Introduction

The flow around a circular cylinder is one of the most widely studied flow cases, both experimentally and numerically. It is applicable to many physical processes, and the definition of the problem is straight-forward. For long and smooth circular cylinders in infinite fluid the solution is a function of the Reynolds number $Re = DU_\infty/\nu$ only, where D is the constant cylinder diameter, U_∞ is the far-field inflow velocity and ν is the kinematic viscosity of the fluid. The flow solution turns unsteady already around Reynolds number $Re \approx 40$ and the wake become three-dimensional when $Re \gtrsim 200$ [1].

Due to the simple problem definition and the relatively complex flow solution, together with a wide range of applications in nature, science and engineering, numerous experiments and simulations have been performed on this case. Although experiments have been performed on cylinders with lengths up to several thousand diameters [2] to completely eliminate the effect of end boundary conditions, this is currently not feasible to replicate in a simulation, even for very low Reynolds numbers. Instead, periodic boundary conditions are used to replicate an 'infinitely long' cylinder. This is an efficient numerical 'trick' to save computational effort. In real life physical experiments this is not possible, since true periodicity cannot be realized in the laboratory.

It has been known for a long time that flow around cylinders are easily influenced by the spanwise boundary conditions, even for large aspect ratios L/D. Szepessy and Bearman [3] performed experiments on cylinders with end-plates and varying distance between the plates, measuring forces and vortex shedding frequencies for the range $8000 < Re < 1.4 \times 10^5$. Norberg [2] studied the influence of very large aspect ratios, up to $L/D = 5000$ in the most extreme cases for the $50 < Re < 4 \times 10^4$. Both used end-plates to reduce the effect of the solid-wall termination of the cylinder. The specific end-plate configuration was first described by Stansby [4] who developed an optimized end-plate design to reduce the change in base suction with varying cylinder lengths. However, no other flow parameters were taken into account during this design process, i.e. no indications were given on how the end plates changes the flow and wake topology.

Zhang et al. [5] used large eddy simulation to study finite length cylinders in proximity to a symmetry plane (i.e. a frictionless surface) in the spanwise direction at $Re = 3900$. They found that the forces on the finite length cylinder was lower than in the infinite length case, with a drag reduction of up to 25%. They also found that the shear layers of the finite cylinder are more stable, leading to a delayed roll-up further downstream. Pereira et al. [6] used RANS and XLES (eXtra Large Eddy Simulation) to study the difference between periodic and symmetry-plane end-wall boundary conditions also for $Re = 3900$. They found a significant difference in integral quantities such as drag coefficient between these two types of boundary conditions. Frölich and Rodi [7] simulated a short cylinder ($L/D = 2.5$) with one end mounted on a solid wall and the other end in the freestream at $Re = 43000$ focusing on exploring the vortex dynamics on this special case. Neither of these references discuss the effect of no-slip end-wall boundary conditions for long cylinders.

Huang et al. [8] considered the end-wall effects on vortex shedding around a circular cylinder at $Re = 100$ in which they studied the difference between slip and no-slip boundary conditions on the spanwise boundaries. They found that for a cylinder of length $6D$ the effect of no-slip boundary conditions substantially altered the vortex shedding in the middle of the channel. However, their low Reynolds number and short spanwise length does not make any useful reference for a turbulent flow case.

But what happens really in an experiment when a cylinder terminate in a no-slip wall, like the wall of a wind tunnel or water tank? In this paper we present simulation results for cylinders with lengths up to 24 diameters and no-slip boundary conditions in the spanwise direction,

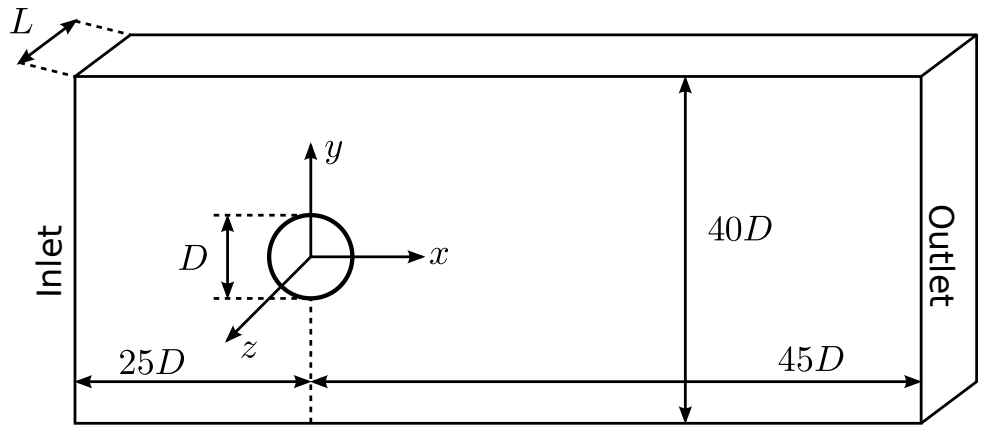

Figure 1: Computational domain and coordinate system. The origin of the coordinate system is in the center of the cylinder. The three directions are named streamwise (x-direction), crossflow (y-direction) and spanwise (z-direction). L is the length of the cylinder and width of domain. The figure is not to scale.

replicating an experimental channel with a cylinder mounted between two parallel solid walls. In addition, we have simulated a cylinder with periodic spanwise boundary conditions as a reference simulation for comparison with other published data.

We have previously studied a particular cylinder with fairings at $Re = 5000$ with both LES, DNS and PIV [9] and studied the influence of boundary conditions on this specific case and aspect ratio $L/D = 12$ [10]. In these studies we limited ourselves to one aspect ratio and one Reynolds number. The geometry we used was equipped with special fairings designed to reduce drag and the oscillating forces from vortex shedding. Since the geometry was unique and never studied before, there were no reference data available from other sources. The present paper is a follow-up on this work, where the case is generalized by removing the fairings and lowering the Reynolds number to $Re = 3900$, making it possible to compare our results with previously published data. We also increase the largest aspect ratio to $L/D = 24$ and include a lower aspect ratio of $L/D = 6$ to give a more complete description of the flow case.

2 Problem and definitions

The computational domain is shown in figure 1. The coordinate system is indicated in the figure, where the x-, y- and z-direction are the streamwise, crossflow and spanwise direction, respectively. The width of the domain equals the length of the cylinder L. All cases have a fixed-velocity inflow boundary condition at the inlet, that is $(u, v, w) = (U_\infty, 0, 0)$ and Neumann condition on the pressure ($\partial p/\partial x = 0$). The outlet condition is a fixed pressure outlet ($p = 0$) with Neumann conditions on all three velocity components. The boundary conditions in the crossflow direction

Table 1: Simulation matrix.

Simulation	per-6D	nos-6D	nos-12D	nos-24D
Cylinder length L	$6D$	$6D$	$12D$	$24D$
Spanwise BC	Periodic	No-slip	No-slip	No-slip
Number of grid cells	76×10^6	76×10^6	152×10^6	304×10^6
Min. $\Delta x/D, \Delta y/D$	0.00625	0.00625	0.00625	0.00625
Min. $\Delta z/D$	0.0125	0.0125	0.0125	0.0125

are that of a symmetry plane, this prescribe zero wall-normal velocity ($v = 0$) and Neumann conditions on all other flow quantities. For all no-slip boundaries (in the spanwise direction and on the cylinder surface) we prescribe zero velocity and a Neumann condition for the pressure.

For the cases with no-slip spanwise boundary conditions, we have simulated three aspect ratios: $L/D = 6$, $L/D = 12$ and $L/D = 24$. For the reference case with periodic conditions, we only simulated $L/D = 6$. Parnaudeau et al. [11] investigated the difference between $L/D = \pi$ and $L/D = 2\pi$ for the same Reynolds number. They found the difference to be small and concluded that a span of πD in many cases could be sufficient. With that in mind, we believe that there is no need for any longer cylinders than $L/D = 6$ when using periodic conditions. The Reynolds number is, as previously noted, $Re = 3900$ in all cases.

The different simulated cases are summarized in table 1. All simulations were run until the effects of the initial condition no longer was present. After this initial phase, statistics were sampled over 2000 D/U_∞ time units, corresponding to roughly 400 vortex shedding cycles (given a Strouhal number of $St \approx 0.2$). The reason for this large number of cycles is to achieve converged statistics along the entire span of the cylinder, without using a spanwise average.

3 Numerical methods

The code *MGLET* [12] has been used to perform all simulations presented in this paper. In short, MGLET uses a finite-volume formulation on staggered grids solving the incompressible Navier-Stokes equations using linear interpolation and integration for all spatial terms, hence leading to second-order accuracy in space. A third-order low-storage explicit Runge-Kutta time integration scheme [13] is used for time stepping.

MGLET uses a staggered Cartesian grid and introduces the solid geometry through an immersed boundary method [14]. A local refinement of the grid around the cylinder is achieved

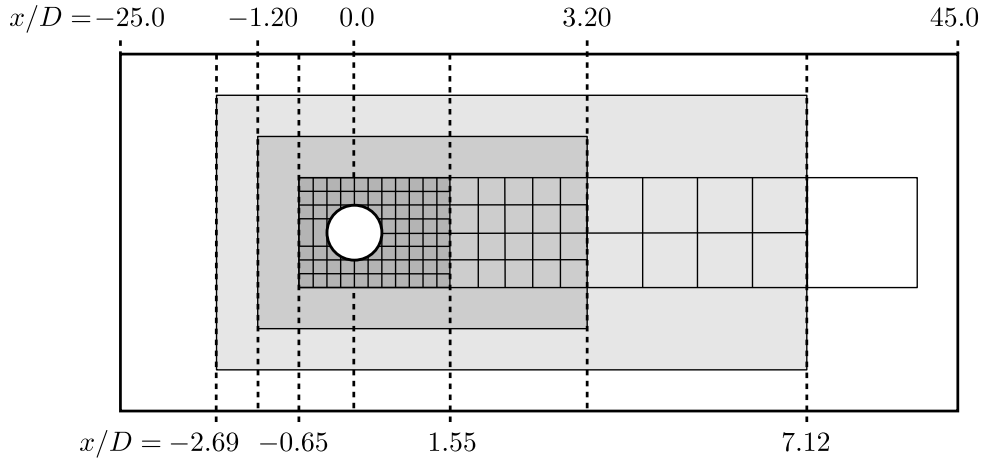

Figure 2: Schematic illustration in 2D of the grid design and refinement process. The grid refinement regions are marked with darker shades of grey for finer regions. Not to scale.

by embedding zonal grids. In the LES presented here, we used three levels of local grid refinement (plus one coarse, parent grid) around the cylinder. This resolves the cylinder, its boundary layers and the wake behind it sufficiently while keeping the total number of grid cells at a reasonable level. The refinement process is a simple cell splitting, in which each parent grid cell subject to refinement is split into eight equal (3-D) child cells [15]. A schematic illustration of the grid design is given in figure 2. The resulting smallest grid cell size is $0.00625D$ in the x- and y-direction and $0.0125D$ in the z-direction. The grid is homogeneous in the spanwise direction. The grids consist of 76, 152 and 304 million grid cells for the three aspect ratios $L/D = 6$, $L/D = 12$ and $L/D = 24$, respectively.

The time step was fixed at 0.002 D/U_∞ in all simulations, except in the initial phase where we used a smaller timestep for stability reasons, but no data was sampled from this phase. This resulted in an average maximum CFL (Courant–Friedrichs–Lewy) number of 0.77, well below half of the stability limit of the time integration method. For comparison, the results by Parnaudeau et al. [11] were simulated with a time step of 0.003 D/U_∞ and a second order time integration method. The 'Wall-Adaptive Local Eddy-viscosity' model, more commonly known as the WALE model [16], was used as the LES subgrid-scale model. The same numerical setup has also been used in other recent works, such as [17].

3.1 Grid convergence

A detailed grid convergence study has been conducted. Four different grids of similar kind but with different resolution were created and the reference periodic case simulated. The overall properties of each grid is provided in table 2. The results in figure 3 clearly show that there

Table 2: Grid convergence study setup

Simulation	coarse	medium	fine	veryfine
Cylinder length L	$6D$	$6D$	$6D$	$6D$
Spanwise BC	Periodic	Periodic	Periodic	Periodic
Number of grid cells	15×10^6	35×10^6	76×10^6	613×10^6
Min. $\Delta x/D, \Delta y/D$	0.025	0.0125	0.00625	0.00312
Min. $\Delta z/D$	0.05	0.025	0.0125	0.00625
Time step Δt	0.002	0.002	0.002	0.001
Time steps	262144	262144	262144	167580

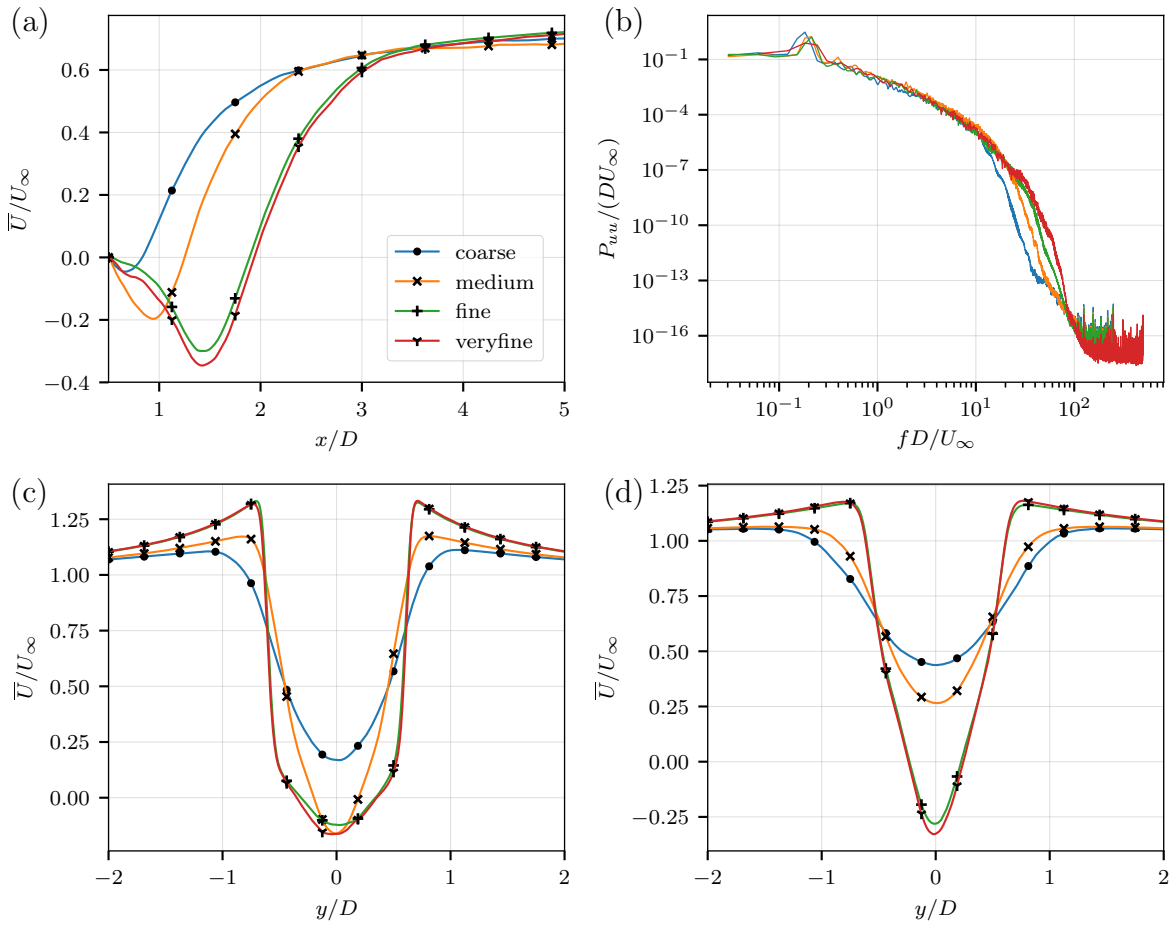

Figure 3: Results from the grid convergence study with the four grids from table 2. (a) time-averaged streamwise velocity in the centerline behind the cylinder at $y = 0$. (b) energy spectra in the point $(x, y, z) = (1.54D, 0.6D, 0.0)$ and (c) and (d) time-average streamwise velocity in two transverse lines at $x/D = 1.06$ (c) and $x/D = 1.54$ (d). All data are sampled in the centerplane at $z = 0$.

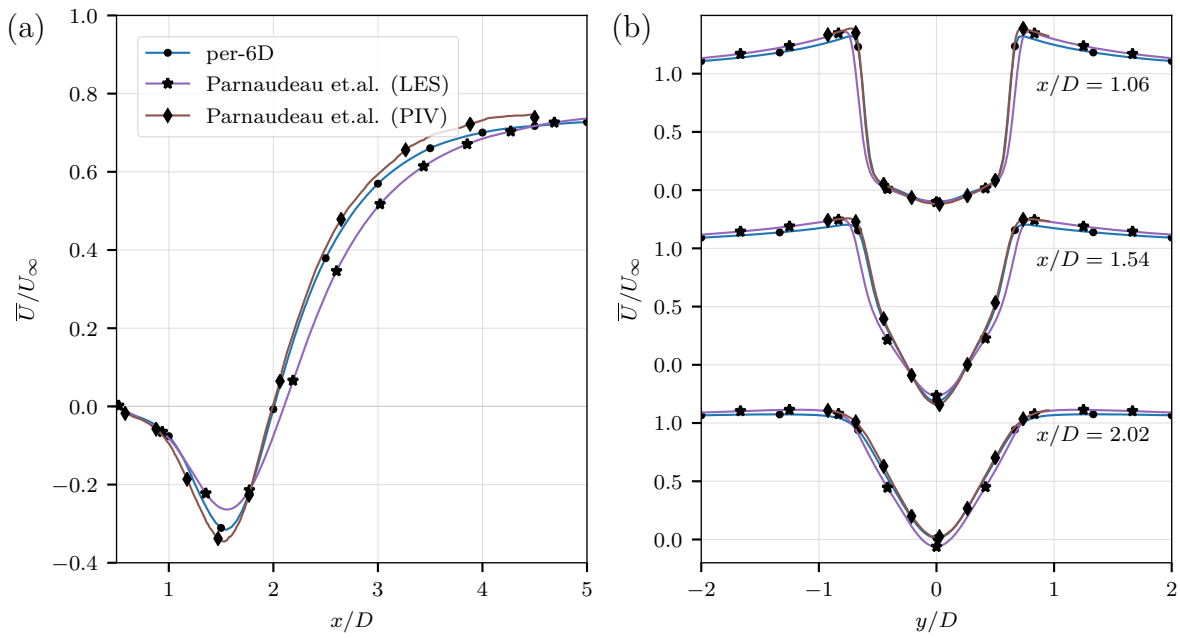

Figure 4: Comparing results from case *per-6D* with data from Parnaudeau et al. [11] (high resolution LES and PIV cases). All lines are sampled in the center plane at $z = 0$.

is only minor difference between the case *fine* and *veryfine*. Since the *veryfine* grid has more than eight times the number of cells and require a time step of half that of the *fine* grid, the computational cost of the *veryfine* grid is more than 16 times that of the *fine*. For this reason the *veryfine*-case was only run a limited time until the first order statistics were converged. The results in figure 3 are very clearly showing that the *fine* and *veryfine* case provide almost identical results. For this reason the *fine* grid was chosen for all further simulations.

3.2 Comparing with references

We have obtained the velocity profile data from Parnaudeau et al. [11]. The reference dataset contain both flow data simulated with LES and experimental data obtained by PIV (particle image velocimetry). A cylinder with end-plates was used in the experiment, and the cylinder length between the end plates were $L/D = 20$. The reference data is plotted together with (the same) data from the current simulation *per-6D* in figure 4. The reference LES dataset exhibits a somewhat higher minimum streamwise velocity at the centerline behind the cylinder, and a slightly lower velocity in the range $1.8 < x/D < 4.0$. The match between our simulations and the experimental PIV data from the same reference [11] is on the other hand excellent. In total, we consider the comparison to be satisfactory, and that all the effects discussed in the remainder of this paper will be much larger than the discrepancies seen in figure 4.

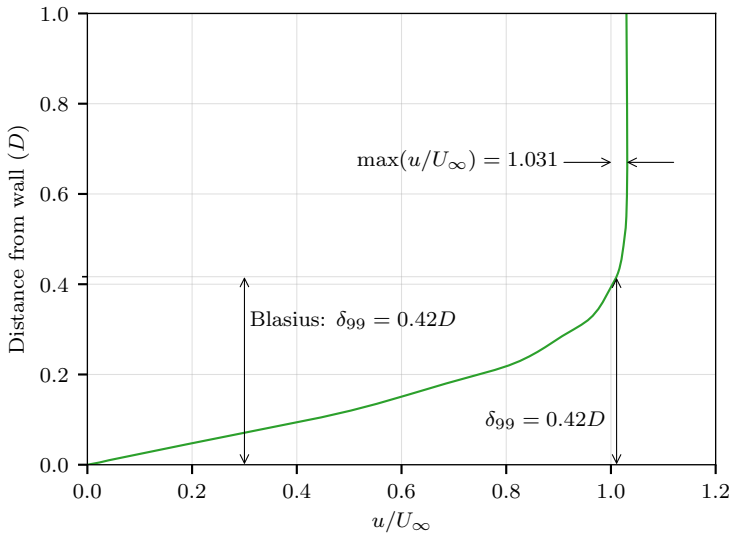

Figure 5: Illustration of boundary layer profile $\overline{U}$ in the empty channel corresponding to case *nos-12D* at position $x = 0$. The Blasius boundary layer thickness defined as the location where $u/U_\infty = 0.99$ is indicated on the figure. The actual boundary layer thickness, defined as the location in which the velocity approach 99% of the value in the center of the channel, is also indicated as δ_{99}. The boundary layer is resolved by approximately 34 grid cells.

3.3 Simulation without body

A parameter in the simulations with the no-slip spanwise boundary conditions is the nature of the boundary layer in the vicinity of the cylinder. If we position the cylinder closer to the (uniform) inlet, it 'sees' a thinner boundary layer compared to a cylinder placed further away. Since the boundary layer is laminar, we can make an estimation of the boundary layer shape based on a Blasius profile. However, due to the coarse grid near the channel inlet the boundary layer profile will deviate from the ideal Blasius solution. In addition, we have a blockage effect due to the displacement of the boundary layers which will contribute to increase the velocity in the center of the domain.

We have performed a simulation with an empty channel, that is without any cylinder present. We used the domain from the intermediate length cylinder case ($L/D = 12$). In this way, we can see how the boundary layers develop without the interference from the cylinder. A velocity profile taken at the location of the cylinder ($x = 0, y = 0$) is presented in figure 5. This shows that there is a large region of nearly uniform velocity u in almost the entire cross-section. The velocity at the center is slightly larger than the inlet velocity U_∞ by about 2.1%. When approaching the walls, the velocity increases from the value in the center of the channel, up to a maximum of 3.1% larger than the inflow velocity $0.67D$ from the wall (indicated in the figure 5 with both position and magnitude). The boundary layer thickness predicted by a Blasius profile for this

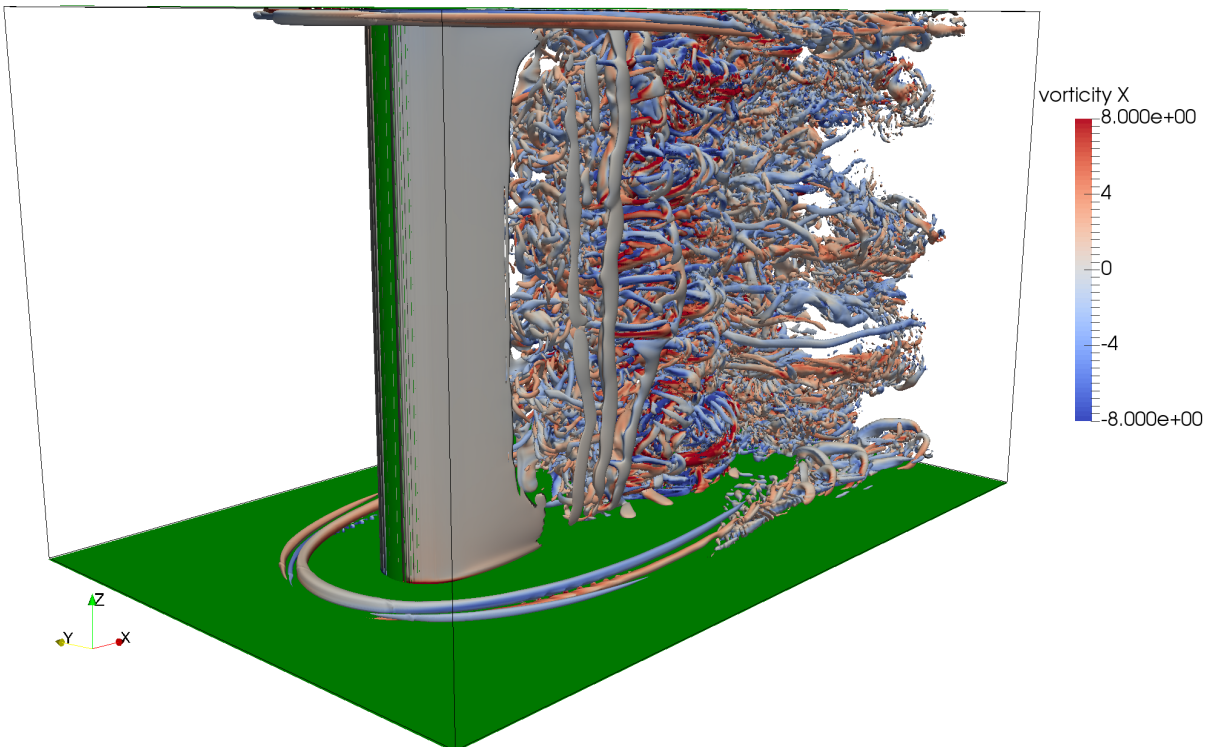

Figure 6: Instantaneous view of the flow field for the 'nos-6D' case showing the cylinder wake and horseshoe vortex system. The solid green surfaces indicate the no-slip boundary conditions on the cylinder itself and the side walls. The isosurfaces are computed for $Q = 2.0$ and coloured by the streamwise vorticity $\omega_x D/U_\infty$.

location in the tank is $\delta_{99} \approx 0.42D$. When we define our boundary layer thickness as the location in which the velocity reach 99 % of the velocity in the center of the channel, we get a computed boundary layer thickness of $\delta_{99} \approx 0.42D$, which happens to be exactly the same as predicted by the Blasius profile.

In total, it seems like the simulation is representing a physical channel flow. The velocity profile is not completely uniform, but in laboratory experiments this will never be the case either. Since the velocity increase in the middle of the channel is small, to keep it simpler, we will normalize all velocities with respect to the inlet velocity U_∞ instead of using the actual velocity in the center of the channel.

4 Results

To give an overview of the flow topology for the cases with no-slip boundary conditions, the Q-criterion was computed for the case 'nos-6D' and is shown in figure 6. The most important feature compared to the flow around an infinitely long cylinder, is the horseshoe vortex system

Table 3: Main flow coefficients. The symbols are explained in the nomenclature in the beginning of the paper. The characteristics from [11] are from the high-resolution LES case and the data from [18] are from 'run 7'. Recirculation length and vortex formation length are measured from the base of the cylinder.

Simulation	per-6D	nos-6D	nos-12D	nos-24D	Ref. [11]	Ref. [18]
St	0.212	0.196	0.208	0.210	0.208	0.210
$\overline{C_D}$	0.968	0.867	0.897	0.904		
C_D^{rms}	0.0258	0.0116	0.0093	0.0123		
C_L^{rms}	0.1249	0.0076	0.0235	0.0224		
$-\overline{C_{pb}}$	0.865	0.699	0.747	0.763		0.900
L_r/D	1.508	2.987	2.250	2.061	1.56	1.198
L_v/D	0.872	2.814	1.615	2.003	0.92	
U_{min}/U_∞	-0.316	-0.389	-0.285	-0.271	-0.26	-0.28

developing around the intersection between the solid wall and cylinder. The figure shows a laminar horseshoe vortex forming around the cylinder, which turns turbulent around $x/D = 3.0$. This point of transition is significantly further downstream than the point of transition in the shear layers separating from the cylinder. The same principle flow configuration with a horseshoe vortex is present in all no-slip cases even though they are not all shown here.

The main flow characteristics and force coefficients are summarized in table 3. The force coefficients presented here are measured and averaged over the entire span of the cylinder. A practical consequence of this is that the ends of the cylinder are within the wall boundary layer in the cases with no-slip boundaries, and consequently the force coefficients are affected by this. The largest difference between the cases with- and without the no-slip spanwise boundary is that the RMS of the lift coefficient C_L^{rms} is dramatically lower in the cases with no-slip boundary condition, compared to the periodic case.

The Strouhal number is calculated based on the time history of the fluid velocity u and v in position $(x, y, z) = (3.0D, 0.45D, 0)$ in the wake. The base pressure coefficient is based on the mean pressure difference between a point immediately behind the cylinder (at $x = 0.5D$) in the center of the domain and a corresponding point upstream at $x = -20D$. For the cases with no-slip boundary conditions, the presence of the no-slip walls will lead to a pressure drop along the channel that will affect the base pressure coefficient.

Figure 7 shows the time-averaged streamwise and spanwise velocities in a slice through $y = 0$. The first important point is that the velocities are nearly perfectly symmetric ($\overline{U}$) and antisymmetric ($\overline{V}$) in the z-direction, which mean that the statistics are well converged

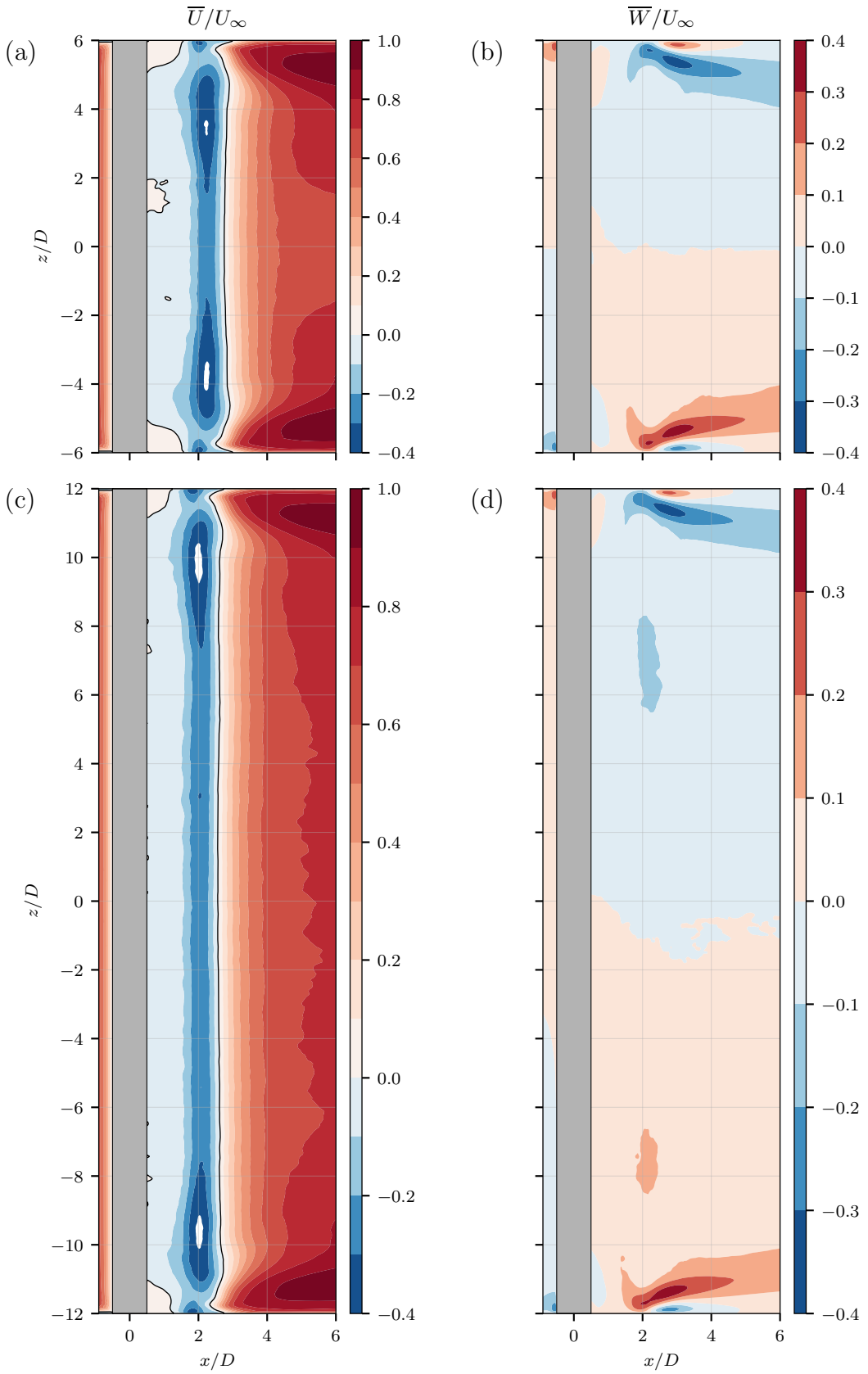

Figure 7: Time-average streamwise (a, c) and spanwise (b, d) velocity in a slice through $y = 0$ for the cases *nos-12D* (a, b) and *nos-24D* (c, d). White regions are regions where the velocity exceed the defined color scale indicated on the colorbar. Blue colors are negative velocities and red colors are positive velocities. The solid black line in plots (a, c) indicate the contour $\overline{U} = 0$.

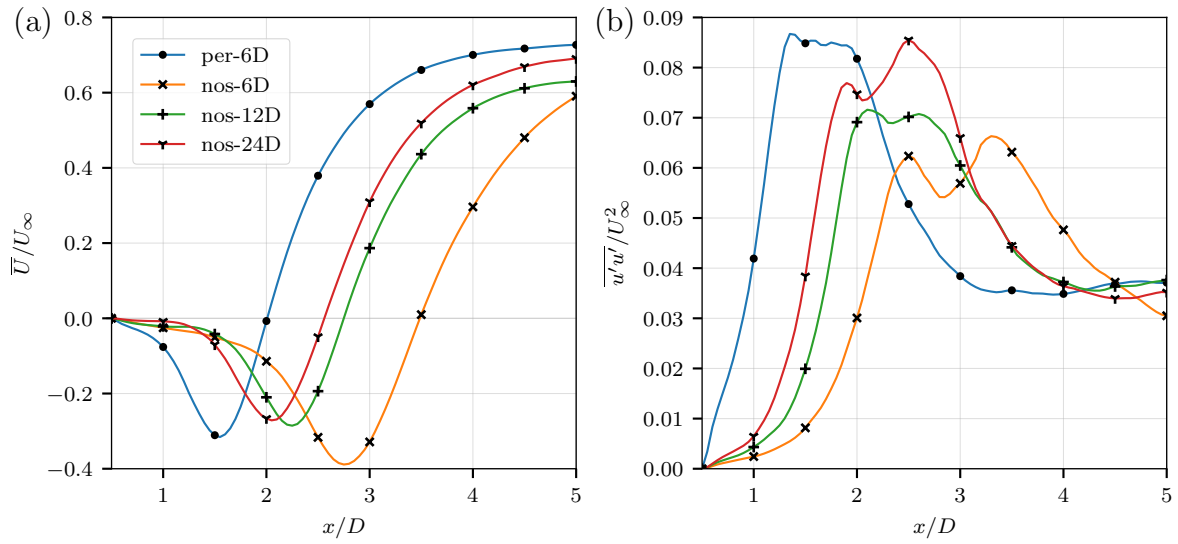

Figure 8: Profiles of mean velocity $\overline{U}$ (a) and $\overline{u'u'}$ (b) along the center line behind the cylinder. The origin of the x-axis is in the center of the cylinder. The lines are sampled in the center of the domain at $z = 0$.

throughout the channel. Secondly, the figure shows that the walls have a significant effect on the mean flow around the cylinder. The extent of the influence is much wider than the boundary layer thickness δ_{99}, from the previous chapter we recall that this is only about $0.4D$. From figure 6 we also recall that the horseshoe vortex system is confined to a region very close to the wall, typically less than $1D$ away. Despite this, the influence of the wall reaches all the way into the channel for the *nos-12D* case as seen in figure 7 (a). The mean streamwise velocities on the other hand, are influenced by the wall up to about $4D$ from the wall. The spanwise velocities have significant non-zero values up to $2D$ away from the walls. In the center of the channel, there is also a wide region with nearly 2-D flow statistics, this region is also about $4D$ wide. This region of influence from the walls is increasing quickly downstream in the wake.

Stäger and Eckelmann [19] studied the thickness of the wall-affected region on a cylinder with various end-plate diameters. If we use their data (provided in [19] figure 9) and assume that our setup is similar to an endplate with diameter $25D$ (the same as the distance from the cylinder to the inflow boundary in the present study), we find that the thickness of the wall-affected region is between $5D$ and $6D$. This fits nicely within both figure 7 (a) and (c). Despite that we see a large region with 2-D flow statistics in figures 7 (c) and (d), the flow is still strongly influenced by the wall throughout the entire domain. The notion of a certain 'wall-affected' region is thus in our opinion misleading.

Figure 8 present the mean streamwise velocity in the centerline behind the cylinder, in the

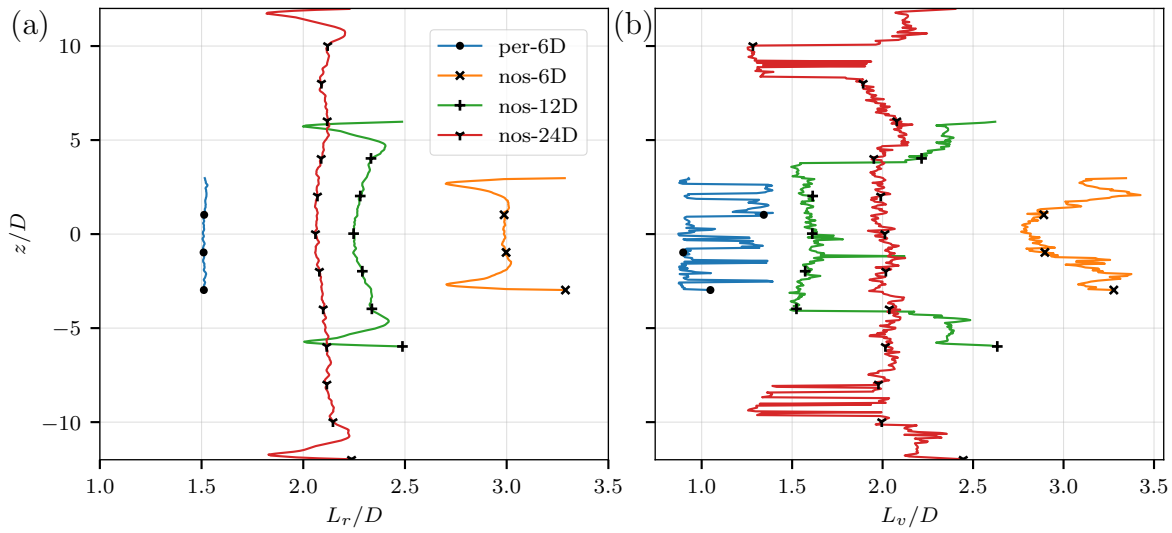

Figure 9: Profiles on how the recirculation length L_r (a) and vortex formation length L_v (b) vary along the span of the cylinder for the different cases.

middle of the domain (at $y = 0$ and $z = 0$) for all simulated cases. This figure shows the major impact of the no-slip boundary condition. All characteristic points, like the recirculation length (the distance from the base of the cylinder to the the point where $\overline{U}$ turns positive) and vortex formation length (the distance from the base of the cylinder to the maximum of $\overline{u'u'}$) is longer by $0.5D$ to $1D$ for all no-slip cases compared to the periodic case.

Another interesting feature is that there is no sign of immediate convergence towards the periodic reference case. Even the *nos-24D* case deviate significantly from the *per-6D* case. We believe that a cylinder length of more than $100D$ is needed before the results are comparable with the periodic reference case. This argument can be made because the difference between the *nos-12D* and *nos-24D* cases are quite small compared to the difference with the *per-6D* case, and hence no sudden convergence can be expected.

The recirculation length and vortex formation length are extracted from every grid cell location in the z-direction along the cylinder span, and plotted in figure 9. Again we see large differences between the cases, even between the $24D$ length cylinder and the periodic case. The recirculation length increase from about $1.5D$ to about $2.1D$ in the center of the channel going from the periodic case to the *nos-24D* case. Both quantities vary only marginally along the cylinder span, and there are huge regions in the center of the channels where these quantities do not change at all. The trend we have commented on earlier is also still present, i.e change from the *nos-12D* to *nos-24D* case is much smaller than the difference compared to the *per-6D* case.

Ma et al. [20] discussed the shape of the streamwise velocity profiles in the very near wake,

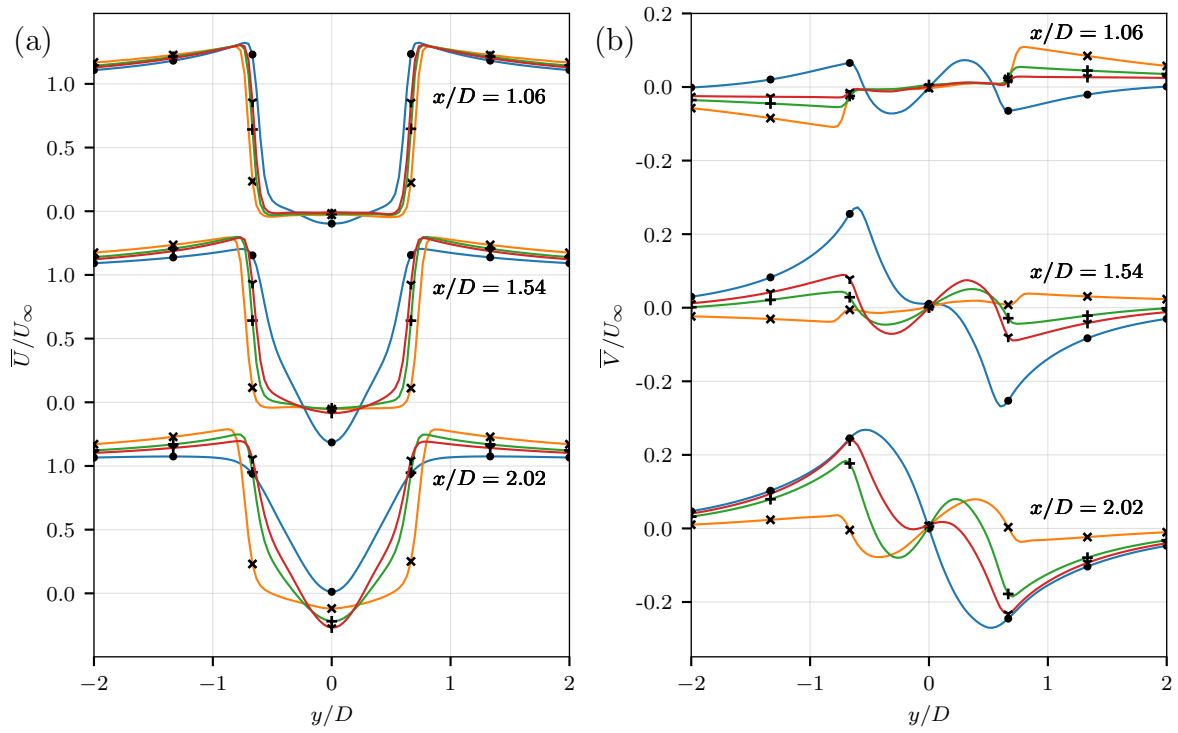

Figure 10: Time-averaged streamwise (a) and crossflow (b) velocity in the wake behind the cylinder at three different locations at $z/D = 0$. For legend, see figures 8 - 9.

and how very small changes in the simulation setup, such as the length of the cylinder and inflow turbulence intensity can trigger a change from a U-shaped velocity profile to a V-shaped velocity profile. Tremblay [21], on the other hand, demonstrated how insufficient sampling can influence the shape of the velocity profiles in the wake, and comment that a lot of the previously published data in this field are probably sampled over too few shedding cycles.

We have plotted the same velocity profiles at the same locations in figure 10. At the nearest section, at $x/D = 1.06$, the shape of the profile is nearly square for all cases with no-slip boundary conditions, with very high crossflow gradients of the mean velocity. The periodic reference case shows a more U-shaped profile. In the middle section at $x/D = 1.54$ the periodic case has turned into a V-shaped profile, the *nos-6D* case is still a square profile and the *nos-24D* case is more like a U-shape. At the section furthest away, all profiles, except the $6D$ case, are clearly V-shaped.

The shear layers forming behind the cylinder is shown in the plot of spanwise vorticity $\overline{\omega_z}D/U_\infty$ in figure 11 for both time averaged and instantaneous values. This figure indicates that the shear layers of the cases with no-slip sidewalls are more stable than in the periodic case. This enhanced stability leads to a delay of the roll-up of the shear layer vortices and subsequent breakdown. If we compare the location of the last negative or positive vorticity contour before

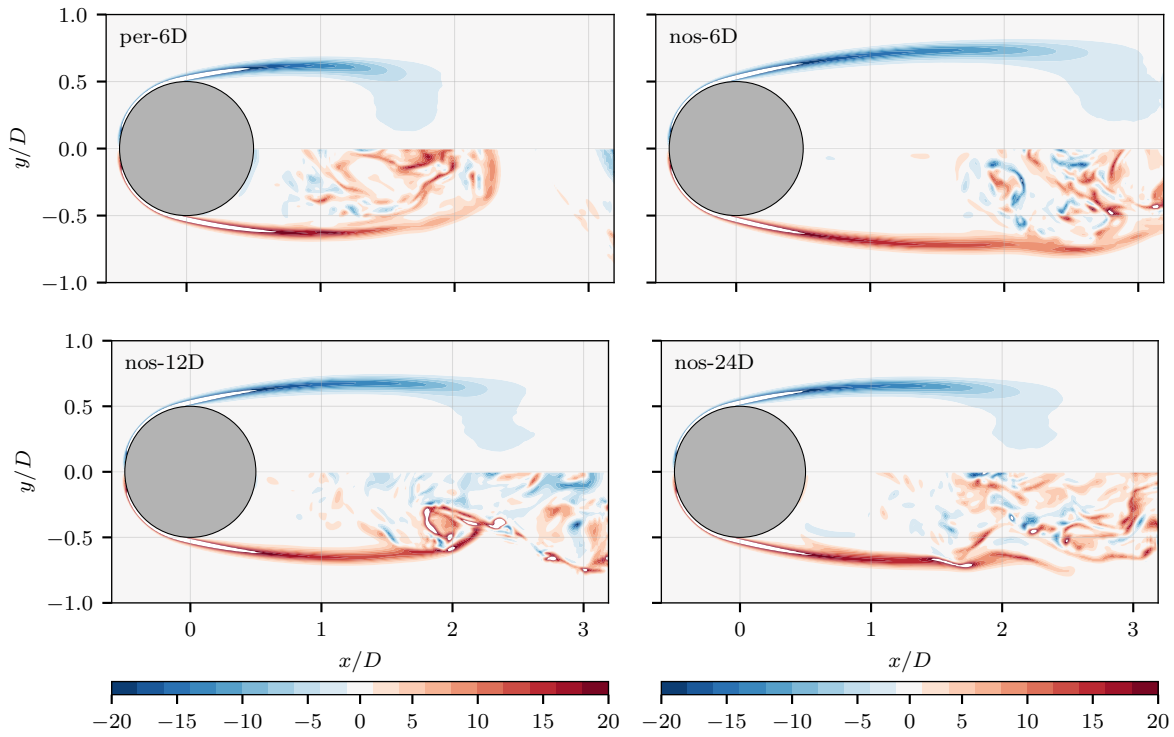

Figure 11: Split view plot: Time-averaged vorticity $\overline{\omega_z} D/U_\infty$ on the top half in each panel, and instantaneous spanwise vorticity $\omega_z D/U_\infty$ in the lower half. Both quantities are sampled in the center of the domain at $z = 0$. The instantaneous values are not in phase with each other and are from the last computed timestep of each simulation.

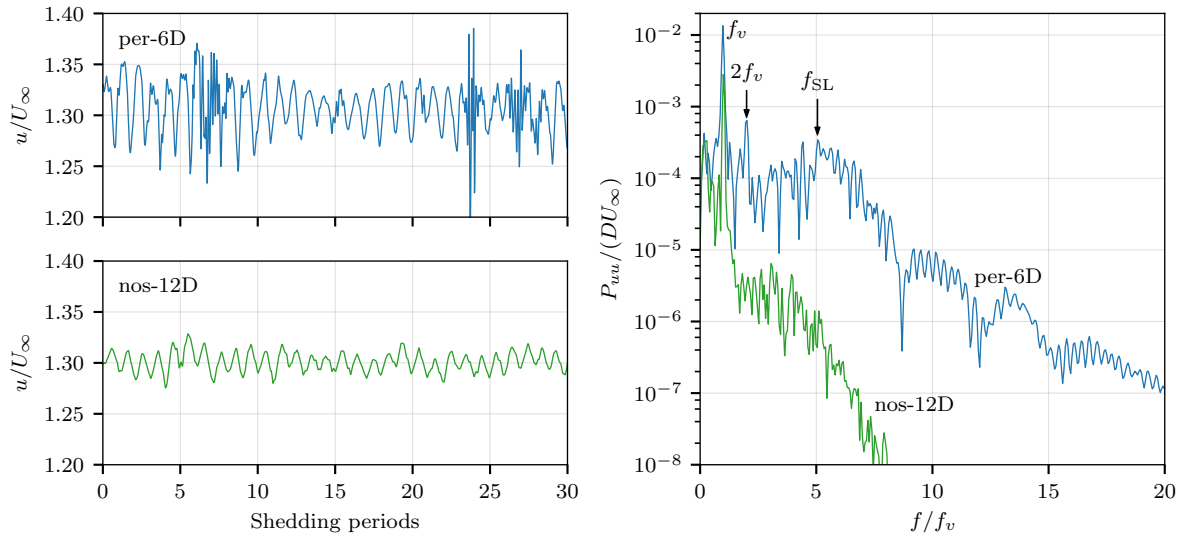

Figure 12: Left: Time traces of instantaneous streamwise velocity u in a point $(x, y, z) = (1.0, 0.8, 0.0)$ shown for 30 vortex shedding cycles. Right: Power spectral density computed with Welch's method [22] of the velocity measurement. The peak corresponding to the shear layer instability is marked f_{SL}.

the white region around the zero contour, we see that this contour extends all the way down to $x/D = 2.5$ in the *nos-24D* case, while in the periodic case this contour stops at $x/D = 1.8$. We also see that the regions with very high vorticity, above and below the color scale in this figure (pure white regions), are more or less of identical shape and size.

To show how the no-slip boundary condition stabilizes the shear layers, we conducted two additional simulations where we sampled the time trace of the velocity in discrete points for the *per-6D* and *nos-12D* cases. The sampling was over slightly more than 40 vortex shedding cycles. The time traces of the streamwise velocity u is shown in figure 12 for the 30 first cycles. We also computed the power spectral density for both time series. The velocity measurements for the case *per-6D* clearly show the same intermittent high-frequency bursts as discussed by Prasad and Williamson [23]. These high-frequency bursts occur at irregular intervals, with frequencies significantly higher than the vortex shedding frequency. The *nos-12D* case does not show any such features at all. The power spectra also shows that the case with no-slip boundary condition contains almost no energy for frequencies higher than the vortex shedding frequency. The *per-6D* case show a distinct high-energy region around $f/f_v = 5$ corresponding to the shear layer instability frequency f_{SL}, and a peak at $f/f_v = 2$ corresponding to the first harmonic of the shedding frequency. Neither of them is visible in the spectrum for the *nos-12D* case. In summary, the power spectrum for the *nos-12D* case is clearly much more narrow-banded than the *per-6D* case at this location in the wake.

5 Concluding Remarks

Our simulations show that even for long cylinders, placement of the cylinder in a channel with no-slip boundary conditions along the walls (e.g. a circulating water tunnel, wind tunnel etc.) gives huge impacts on the flow, also in the centre of the channel, far from the wall boundary layers.

The shear layers forming behind the cylinder are considerably more stable in the simulation with the no-slip walls, and this delays the roll-up and formation of the turbulent wake. This is seen both on the mean and instantaneous vorticity and on the time-trace of a velocity sampling just outside of the shear layer. For the case with no-slip walls there is significantly less energy content for higher frequencies compared to the case with periodic boundary conditions. These effects must be considered when designing experiments and also when comparing experimental and simulation results.

Another important result is that we showed that even though there is large regions of two-dimensional flow statistics in the center of the channel, this is not alone enough to claim that the results are independent of the aspect ratio or free of any end-wall effects. Our *nos-24D* case show that even tough there is a 12D wide region of 2-D flow statistics in the center of the channel, the flow statistics there are not representative for the reference case with periodic boundary conditions, i.e. for an infinitely long cylinder.

6 Attached animation

An animation of the shedding process in the periodic case is attached to the electronic version of this paper. The data and time series are the same as shown in figure 12. The reason for the high-frequency bursts are much more clearly visible in this animation than in the still images in figure 11. The black crosses in the animation indicate the position of the velocity sampling.

7 Acknowledgments

The authors wish to thank the employees at *KM Turbulenz GmbH* for all their help and technical support on the MGLET code. Computing time was granted by the *Leibniz Computing Center* (LRZ) of the *Bavarian Academy of Sciences* under project *pr84gi* and UNINETT Sigma2 under project *nn9191k*. We appreciate the effort of P. Parnadeau, J. Carlier, D. Heitz and E. Lamballais

for making the data from [11] available to us in numerical form.

The constructive suggestions and tips from the anonymous reviewers was crucial to improve the quality of the final paper.

References

[1] B. M. Sumer and J. Fredsøe. *Hydrodynamics Around Cylindrical Structures*. Advanced Series on Ocean Engineering. World Scientific, 2006. ISBN: 9812700390.

[2] C. Norberg. 'An experimental investigation of the flow around a circular cylinder: influence of aspect ratio'. *Journal of Fluid Mechanics* 258 (Jan. 1994), pp. 287–316. DOI: 10.1017/S0022112094003332.

[3] S. Szepessy and P. W. Bearman. 'Aspect ratio and end plate effects on vortex shedding from a circular cylinder'. *Journal of Fluid Mechanics* 234 (Jan. 1992), pp. 191–217. DOI: 10.1017/S0022112092000752.

[4] P. Stansby. 'The effects of end plates on the base pressure coefficient of a circular cylinder'. *Aeronautical Journal* 78 (Jan. 1974), pp. 36–37. DOI: 10.1017/S0001924000036319.

[5] H. Zhang, J.-M. Yang, L.-F. Xiao and H.-N. Lü. 'Large-eddy simulation of the flow past both finite and infinite circular cylinders at Re= 3900'. *Journal of Hydrodynamics, Ser. B* 27 (2) (2015), pp. 195–203. DOI: doi:10.1016/S1001-6058(15)60472-3.

[6] F. S. Pereira, G. Vaz and L. Eca. 'Flow past a circular cylinder: a comparison between RANS and hybrid turbulence models for a low Reynolds number'. In: *34th International Conference on Ocean, Offshore and Arctic Engineering*. OMAE2015-41235. St. John's, Canada, June 2015.

[7] J. Fröhlich and W. Rodi. 'LES of the flow around a circular cylinder of finite height'. *International Journal of Heat and Fluid Flow* 25 (3) (2004), pp. 537–548. DOI: doi.org/10.1016/j.ijheatfluidflow.2004.02.006.

[8] Z. Huang, H. I. Andersson and W. Cui. 'End-wall effects on vortex shedding in planar shear flow over a circular cylinder'. *Computers & Fluids* 42 (1) (Mar. 2011), pp. 102–107. ISSN: 0045-7930. DOI: 10.1016/j.compfluid.2010.10.009.

[9] H. Strandenes, J. P. Gallardo, J. Visscher, B. Pettersen, H. I. Andersson, H. Lie and R. Baarholm. 'A comparative study between DNS, LES and PIV for a marine riser with fairings'. In: *34th International Conference on Ocean, Offshore and Arctic Engineering*. OMAE2015-41494. St. John's, Canada, June 2015.

[10] H. Strandenes, J. P. Gallardo, B. Pettersen and H. I. Andersson. 'On the Effect of Boundary Conditions on the Flow around a Cylinder in a Channel'. In: *Proceedings of MekIT'15 Eighth National Conference on Computational Mechanics*. Ed. by B. H. Skallerud and H. I. Andersson. International Center for Numerical Methods in Engineering (CIMNE), 2015, pp. 343–357. ISBN: 97884944244-96.

[11] P. Parnaudeau, J. Carlier, D. Heitz and E. Lamballais. 'Experimental and numerical studies of the flow over a circular cylinder at Reynolds number 3900'. *Physics of Fluids* 20 (8) (2008), p. 085101. ISSN: 1070-6631. DOI: 10.1063/1.2957018.

[12] M. Manhart, F. Tremblay and R. Friedrich. 'MGLET: a parallel code for efficient DNS and LES of complex geometries'. In: *Parallel Computational Fluid Dynamics - Trends and Applications*. Ed. by C. B. Jenssen et al. Elsevier Science B.V., 2001, pp. 449–456.

[13] J. H. Williamson. 'Low-storage Runge-Kutta schemes'. *Journal of Computational Physics* 35 (1) (Mar. 1980), pp. 48–56. DOI: 10.1016/0021-9991(80)90033-9.

[14] N. Peller, A. L. Duc, F. Tremblay and M. Manhart. 'High-order stable interpolations for immersed boundary methods'. *International Journal for Numerical Methods in Fluids* 52 (11) (Apr. 2006), pp. 1175–1193. ISSN: 1097-0363. DOI: 10.1002/fld.1227.

[15] M. Manhart. 'A zonal grid algorithm for DNS of turbulent boundary layers'. *Computers & Fluids* 33 (3) (Mar. 2004), pp. 435–461. ISSN: 0045-7930. DOI: 10.1016/s0045-7930(03)00061-6.

[16] F. Nicoud and F. Ducros. 'Subgrid-scale stress modelling based on the square of the velocity gradient tensor'. *Flow, Turbulence and Combustion* 62 (3) (Sept. 1999), pp. 183–200. DOI: 10.1023/A:1009995426001.

[17] W. Schanderl and M. Manhart. 'Reliability of wall shear stress estimations of the flow around a wall-mounted cylinder'. *Computers & Fluids* 128 (2016), pp. 16–29. DOI: doi.org/10.1016/j.compfluid.2016.01.002.

[18] B. N. Rajani, A. Kandasamy and S. Majumdar. 'LES of flow past circular cylinder at Re = 3900'. *Journal of Applied Fluid Mechanics* 9 (3) (2016), pp. 1421–1435.

[19] R. Stäger and H. Eckelmann. 'The effect of endplates on the shedding frequency of circular cylinders in the irregular range'. *Physics of Fluids A: Fluid Dynamics* 3 (9) (1991), pp. 2116–2121. DOI: 10.1063/1.857894.

[20] X. Ma, G.-S. Karamanos and G. E. Karniadakis. 'Dynamics and low-dimensionality of a turbulent near wake'. *Journal of Fluid Mechanics* 410 (May 2000), pp. 29–65. DOI: 10.1017/S0022112099007934.

[21] F. Tremblay. 'Direct and large-eddy simulation of flow around a circular cylinder at subcritical Reynolds numbers'. PhD thesis. Technische Universität München, 2001.

[22] P. D. Welch. 'The use of fast Fourier transform for the estimation of power spectra: A method based on time averaging over short, modified periodograms'. *IEEE Transactions on audio and electroacoustics* 15 (2) (June 1967), pp. 70–73. DOI: 10.1109/TAU.1967.1161901.

[23] A. Prasad and C. H. Williamson. 'The instability of the shear layer separating from a bluff body'. *Journal of Fluid Mechanics* 333 (Feb. 1997), pp. 375–402. DOI: 10.1017/S0022112096004326.